Automated Detection of Marine Glacier Calving Fronts Using the 2-D Wavelet Transform Modulus Maxima Segmentation Method

Julia Liu [ID], Ellyn M. Enderlin, Hans-Peter Marshall, and Andre Khalil

Abstract—Changes in the calving front position of marine-terminating glaciers strongly influence the mass balance of glaciers, ice caps, and ice sheets. At present, quantification of frontal position change primarily relies on time-consuming and subjective manual mapping techniques, limiting our ability to understand changes to glacier calving fronts. Here we describe a newly developed automated method of mapping glacier calving fronts in satellite imagery using observations from a representative sample of Greenland's peripheral marine-terminating glaciers. Our method is adapted from the 2-D wavelet transform modulus maxima (WTMM) segmentation method, which has been used previously for image segmentation in biomedical and other applied science fields. The gradient-based method places edge detection lines along regions with the greatest intensity gradient in the image, such as the contrast between glacier ice and water or glacier ice and sea ice. The lines corresponding to the calving front are identified using thresholds for length, average gradient value, and orientation that minimize the misfit with respect to a manual validation data set. We demonstrate that the method is capable of mapping glacier calving fronts over a wide range of image conditions (light to intermediate cloud cover, dim or bright, mélange presence, etc.). With these time series, we are able to resolve subseasonal to multiyear temporal patterns as well as regional patterns in glacier frontal position change.

Index Terms—Computational infrastructure, Cryosphere, geographic information systems (GIS), optical data.

I. INTRODUCTION

GLACIER mass loss and thermal expansion are the two largest contributors to contemporary sea level rise, which critically impacts the coastal populations [13]. Global sea level rise is of major concern to the coastal systems, with many communities focusing on the infrastructure adaptations [13]. Estimates of global sea level rise will be critical to risk assessment and the development of adaptation strategies. In addition, the fresh water flux associated with glacier mass loss directly impacts marine ecosystems and regional ocean circulation patterns [28], [37]. Ice mass loss from Greenland's glaciers,

ice caps, and ice sheet contributes ∼43% to the contemporary global sea level rise [30]. The Greenland ice sheet, the largest contributor to sea level rise in the twenty-first century [18], was responsible for an average of $\sim 0.47 \pm 0.23$ mm · yr^{-1} of sea level rise over 1991–2015 [38].

Changes to the terminus position (i.e., calving front position) of marine-terminating glaciers influence glacier mass balance through the direct loss of mass at the calving front. In addition, loss of mass at the glacier terminus modulates the forces governing the glacier ice flow [10], [12]. Loss of the resistive stress generated at the terminus can result in acceleration and thinning of the ice, contributing further to "dynamic" glacier mass loss [3]–[6], [12], [25], [27]. Prior analyses of glacier terminus position change and its influence on the dynamics and mass loss relied on manual mapping of glacier calving fronts (see [5], [21], [27]), which is time intensive and dependent on human interpretation. The accuracy of these manual delineations may drift over time for each analyst and may introduce biases when multiple analysts contribute to data sets. Automated methods for delineating glacier calving fronts are more efficient, repeatable, and objective.

Previously published automated glacier terminus detection methods were based on image classification using various multispectral image bands (see [29], [31], [35]) and simple edge detection methods (see [34]). The application of multispectral band ratios for image classification, such as the normalized difference snow index (NDSI) or normalized difference water index (NDWI), can be applied with reasonable success to the satellite images acquired in months of the year when the snow cover does not extend beyond the glacier margins [31], [35]. However, the seasonal variability in snow cover directly affects the mapped glacier area and may result in large errors in delineation of the ice margin when applied at other times of the year, which limits the temporal resolution of these studies [31]. Furthermore, these image classification techniques require additional processing (e.g., thresholding and vectorization) to identify the continuous regions or boundaries within the image, which can introduce additional errors [32]. The use of gradient-based edge detection algorithms mitigates this processing step. Seale *et al.* [34] developed an automated method to identify the glacier terminus positions using a simple Canny edge detector, which identified largest gradients in image brightness along a glacier flow line. While this method

was successfully applied to the glaciers in the study, the method has not been adopted for other glacier terminus change studies and does not measure positions at other locations along the width of the glacier terminus (i.e., other than along the glacier centerline).

In order to efficiently and objectively quantify changes in the length of marine-terminating glaciers in a more robust manner, we adapt an automated image segmentation technique used previously in a wide variety of applied science fields called the 2-D wavelet transform modulus maxima (WTMM) segmentation method [17]. This edge detection method calculates 2-D gradients in the image brightness and is applied at a variety of spatial scales. The 2-D WTMM segmentation method places 1-pixel thick lines representing contours in intensity change for each spatial scale of analysis. We apply the method to analyze panchromatic Landsat satellite images, chosen for their high image acquisition frequency and radiometric resolutions, of marine-terminating glaciers. This gradient-based and multiscale automated delineation method allows for the detailed analysis of glacier terminus position changes at hundreds to thousands of time points. With the delineations from this method, we generate time series of terminus positions for several glaciers peripheral to the Greenland Ice Sheet. The glaciers along Greenland's periphery are one of the largest contributors to global glacier ice loss [36], yet their contributions to sea level rise through terminus position and associated dynamic changes have not yet been quantified.

II. Methodology

In order to efficiently analyze hundreds of images for each marine-terminating glacier, we developed an automated image processing technique to map the calving front positions. Images were analyzed over the Landsat 8 record (2013–2020) available from the US Geological Survey (USGS) on the Amazon Web Services (AWS) cloud. Ten glaciers were chosen to represent the distribution in size, morphology, fjord geometry, and sea ice conditions at the terminus for the 641 marine-terminating glaciers that are peripheral to the Greenland ice sheet (Fig. 1). The peripheral marine-terminating glaciers were identified based on their Randolph Glacier Inventory (RGI) classifications. Although we focus on Greenland, these conditions are broadly representative of conditions across Arctic glaciers and glaciers along the Antarctic Peninsula.

Aside from the Landsat images, the only inputs required for our automated workflow are (1) a bounding box for the glacier terminus; (2) the Landsat scene boundaries available through the USGS; and (3) an ice velocity map. The glacier bounding boxes (i.e., terminus boxes) were manually drawn to span the narrowest portion of the glacier terminus, in line with the traditional box method for mapping termini [12], [20], [27]. The lengths of the boxes encompass the glaciers' recent terminus positions and extend several kilometers inland in order to account for potential retreat. The Landsat scene boundaries file was downloaded from the USGS (https://www.usgs.gov/media/files/Landsat-wrs-2-scene-boundaries-kml-file). For ice velocities, we used the MEaSUREs 1995-2015 Greenland Ice Sheet Velocity Mosaic
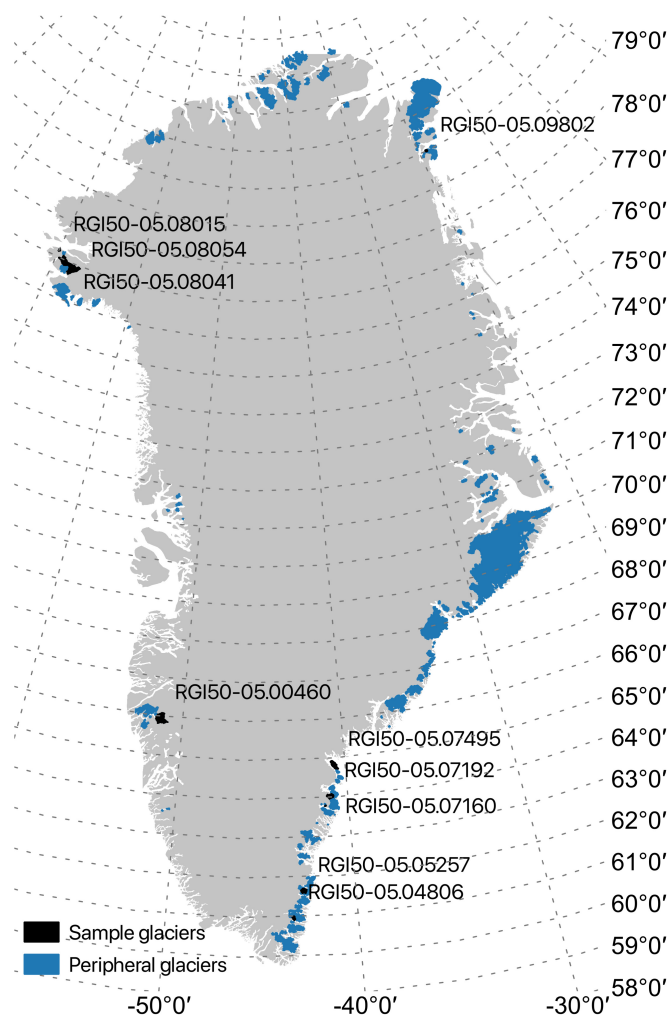

Fig. 1. RGI polygons of the 641 marine-terminating glaciers around Greenland's periphery. Locations of the ten sample glaciers identified for method development are indicated in black and labeled with their RGI IDs.

available at 250-m pixel resolution [14], [15]. The use of a time-averaged velocity data set was preferred over velocities derived from a single-year or less to minimize the effects of random errors and data gaps on our processing pipeline, particularly in regions of slow-flowing ice.

Fig. 2 summarizes the steps used to process these downloaded satellite image subsets. The Landsat images available through AWS are Collection 1 Level-1 Precision and Terrain Correction (L1TP) and Systematic Terrain Correction (L1GT) data products from the Landsat 8 Operational Land Imager (OLI)/Thermal Infrared Sensor (TIRS).

To reduce the computational effort, the Landsat images are subset using buffered terminus boxes. The use of the buffer ensures that the automated delineations are not influenced by edge effects from the 2-D WTMM analysis. The buffer size corresponds to the maximum dimension (either length or width) of the terminus box. The subset 15-m resolution panchromatic Landsat images that fully overlap each terminus box, excluding images with >20% cloud cover in the terminus box, are automatically downloaded from AWS [Fig. 2(a)]. The cloud confidence classification provided in the Landsat Quality
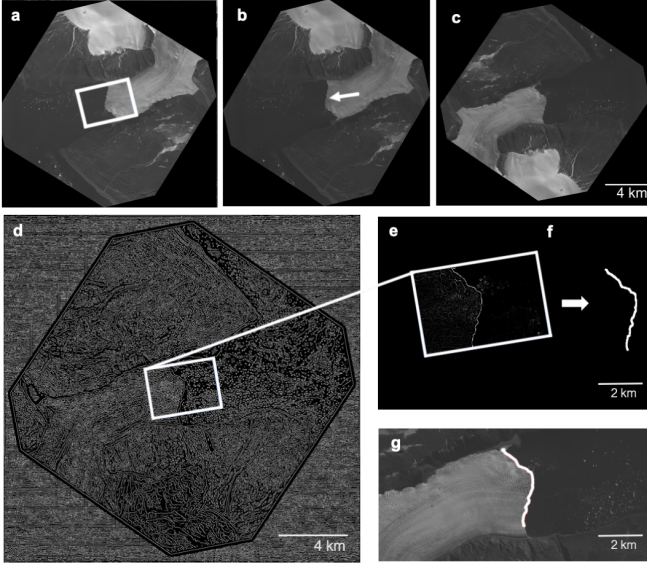
Fig. 2. Image processing steps shown for a Landsat 8 image acquired on August 25, 2018, of peripheral glacier RGI50-05.08054 (76.8639° N, 67.5921° W). (a) Download subset Landsat 8 panchromatic image using a buffer around the terminus box (white). (b) Calculate average glacier flow direction (white arrow) using a velocity map. (c) Rotate image so that flow direction is due right. (d) Generate maxima chains along regions of the greatest intensity gradients using the 2-D WTMM. (e) Examine chains within terminus box extent only (chain's brightness corresponds to gradient value). (f) Eliminate other chains based on length, average gradient value, and orientation. (g) Final terminus delineation. Steps (d)–(g) performed at 50 spatial scales (7–209 pixels).

Assessment (QA) band is automatically used to determine the fraction of pixels within the terminus box that correspond to high cloud confidence. If greater than 20% of the pixels are high cloud confidence pixels, the image is not downloaded. For each terminus box [Fig. 2(a)], we calculate each glacier's average flow direction [Fig. 2(b)] weighted by flow speed. These weighted average flow directions are calculated using the velocity values from the ice velocity raster cropped to the glaciers' RGI outlines. The glaciers' weighted average flow directions are then used to rotate the images so that ice flow is primarily to the right [Fig. 2(c)], as done in [34]. This rotation establishes a common frame of reference for examining terminus changes in which increased distance from the left margin of the box corresponds to terminus advance and decreased distance corresponds with retreat.

The rotated image subsets are then analyzed using the 2-D WTMM segmentation method described in detail in Section II-A. Briefly, the WTMM method identifies points in the image that represent the maximum intensity gradients at the size scale of analysis. These points, named maxima points, are connected in lines called maxima chains that correspond to the regions with greatest intensity gradients throughout the image [Fig. 2(d)]. The maxima chains are generated across 50 size scales ($\sim$100 m–3 km) and then the chain properties (connected or open, length, average gradient value, and orientation) are used to eliminate chains that do not correspond to the glacier terminus [Fig. 2(e)]. From the remaining lines, we choose the most likely terminus delineation [Fig. 2(f) and (g)]. Section II-A describes this method in further detail, Section II-B describes the filtering of the maxima

chains, and Section II-C describes the construction of terminus position time series.

A. Adaptation of 2-D WTMM Segmentation Method

The satellite images over the glaciers are analyzed using the 2-D WTMM segmentation method developed to perform automatic image segmentation for a variety of images across scientific fields including biomedicine, solar physics, astrobiology, etc. [2], [9], [16], [17], [22], [23], [33]. The 2-D WTMM segmentation method is a multiscale, gradient-based method that identifies contours representing the locally maximal changes in the intensity of an image. This is achieved by using the first-order (Gaussian) derivative of the 2-D smoothing function [17]

$$\phi(\vec{x}) = \exp\left(-\frac{|\vec{x}|^2}{2}\right) \tag{1}$$

where $\vec{x}$ represents the point (x_1, x_2) in the image and $|\vec{x}| = (x_1^2 + x_2^2)^{1/2}$. The continuous wavelet transform of the image f is calculated with respect to the partial derivatives of the smoothing function ϕ with respect to x_1 and x_2

$$\psi_1(\vec{x}) = \frac{\partial \phi(\vec{x})}{\partial x_1} \text{ and } \psi_2(\vec{x}) = \frac{\partial \phi(\vec{x})}{\partial x_2} \tag{2}$$

which amounts to taking the gradient of the convolution of the image with ϕ

$$T_\psi[f](\vec{b}, a) = (T_{\psi_1}, T_{\psi_2}) = \nabla(\phi * f) \tag{3}$$

where $*$ represents convolution, $\vec{b}$ represents the parameter of position, a represents a scale parameter, and T_{ψ_1}, T_{ψ_2} are the two components of the wavelet transform

$$T_{\psi_1}[f] = \frac{1}{a^2} \int d^2\vec{x}\, \psi_1\left(\frac{\vec{x} - \vec{b}}{a}\right) f(\vec{x})$$

and

$$T_{\psi_2}[f] = \frac{1}{a^2} \int d^2\vec{x}\, \psi_2\left(\frac{\vec{x} - \vec{b}}{a}\right) f(\vec{x}). \tag{4}$$

The wavelet transform (T_ψ) is a gradient vector which has a magnitude (i.e., wavelet transform modulus, M_ψ) corresponding to the gradient in intensity and a direction (i.e., argument, A_ψ) that points to the highest intensity regions, which are expressed in polar coordinates as

$$M_\psi[f] = \sqrt{\left(T_{\psi_1}[f]^2 + T_{\psi_2}[f]^2\right)}$$

and

$$A_\psi[f] = Arg\left(T_{\psi_1}[f] + iT_{\psi_2}[f]\right). \tag{5}$$

Maxima points represent the regions in the image where the intensity gradients (i.e., moduli) are maximal. WTMM are automatically connected along the maxima chains that act as the edge detection lines for the change in the intensity [Fig. 3(d)]. The algorithmic procedure leading to the calculation of these one-pixel thick maxima chains is outlined in [23, Appendix]. These maxima chains are generated at
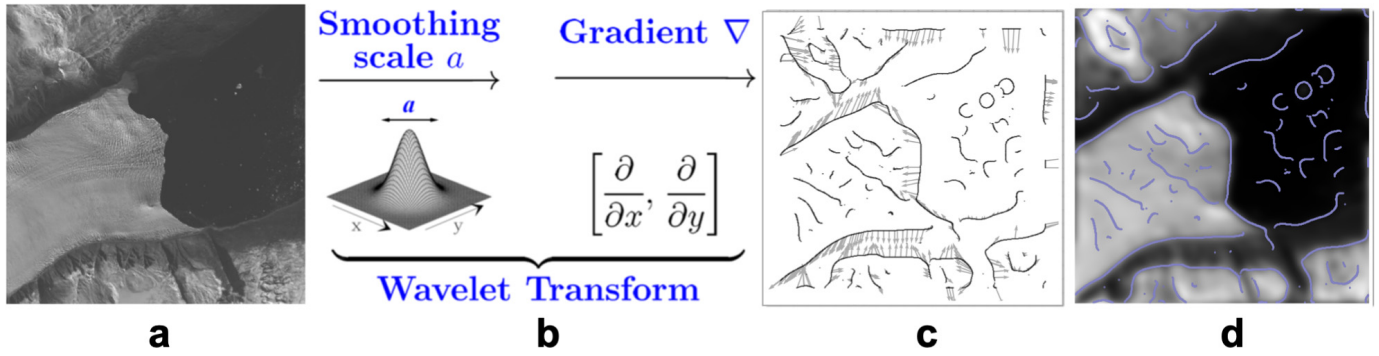
Fig. 3. 2-D WTMM segmentation method on a (a) panchromatic Landsat 8 image acquired on September 14, 2013, of peripheral glacier RGI50-05.08054 (76.8639° N, 67.5921° W). (b) Wavelet transform calculates derivative of a 2-D Gaussian smoothing function and produces gradient vectors throughout the image. (c) Gradient vectors (arrows) and maxima points (dark gray) corresponding to maximal brightness gradients throughout the image at one size scale of analysis. (d) Final brightness gradient contours (i.e., maxima chains) shown over smoothed image.
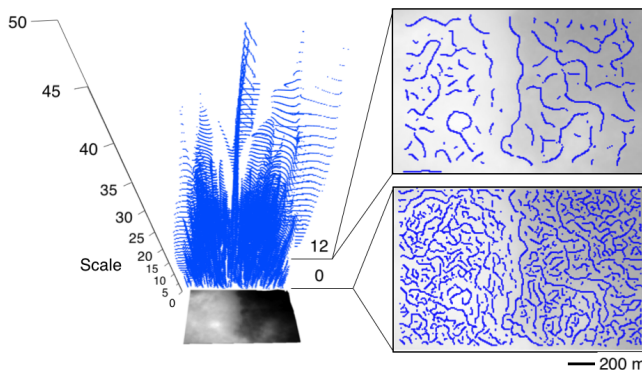

Fig. 4. 3-D skeleton plot showing maxima chains generated from 2-D WTMM analysis of the underlying cloudy image of a glacier terminus at 50 spatial scales, with scale parameter a on the vertical axis. Panels show maxima chains at scales 0 and 12. Chains capture more detail at smaller scales while smaller scale features, such as noise, are smoothed at larger scales.

50 spatial scales ($a = 0, 1, 2, 3, \ldots, 49$) that range from the minimum scale required to resolve the wavelet, $7*2^{0/10} = 7$ pixels, to $7*2^{49/10} = 209$ pixels, corresponding to a range of 105–3135 m in the 15-m resolution Landsat 8 panchromatic images. For the best results, glaciers wider than 105 m should be analyzed with this method.

In the satellite images of the glaciers, the 2-D WTMM calculates intensity gradients using the raw digital number in the pixels and generates maxima chains along the regions with high-intensity contrasts, such as the contrast between glacier ice and sea ice, open water, and land. The multiscale analysis allows for delineation of small-scale and large-scale features (Fig. 4) that allow the algorithm to adaptively delineate glacier termini of variable sizes, geometries, and environmental conditions without *a priori* knowledge of the image conditions [17].

B. Maxima Chain Filtering

Once all the maxima chains outside of the terminus box are removed, we objectively select the final maxima chain corresponding to the glacier terminus using the maxima chains' attributes. The properties for each chain include shape (closed or open), length (L), average modulus value of all maxima points (m), and arguments of the maxima points, which represent the chain's orientation. The closed loops are eliminated immediately, since the glacier termini are open linear features in the terminus box. The remaining attributes are extracted at each scale and objective thresholds are applied sequentially to filter the maxima chains. Generally, the maxima chain delineating the glacier terminus will have a high average modulus value (i.e., large-intensity contrast) and will be longer than most other chains, especially those corresponding to noise but also including features such as crevasses. Orientation is also used to filter the maxima chains because the glacier terminus should be primarily oriented vertically in the rotated reference frame, such that maxima points will mostly have arguments pointing left or right. The threshold for argument is applied to the fraction of arguments that make up each chain and the threshold for length is normalized by the maximum chain length determined for the image, so that the same thresholds can be applied to wide or narrow glaciers. Similarly, the threshold for average modulus value is normalized by the maximum average modulus value determined for the image, so that the same threshold can be applied to images with high- or low-intensity contrasts.

In order to objectively determine the filtering sequence and thresholds used for filtering, we constructed a data set consisting of 512 manual terminus delineations for 5 of the 10 sample glaciers chosen for their diverse morphologies (see Fig. 1 for additional information). For threshold optimization, we randomly allocate 90% of the manual delineations to a training data set and the remaining 10% to a test data set for cross validation. We perform the cross validation four times and report the average errors from the four iterations. Using the training data set, we constrain the length, modulus, and argument thresholds (C_L, C_m, and C_A, respectively) using an optimization technique that minimizes a cost function (Θ) that represents the misfit between the automated delineations and the manual delineations. The misfit for each image (i.e., timepoint) of analysis is the average difference between the automatically and manually delineated terminus positions along three glacier flow lines at one-quarter, one-half, and three-quarters of the width of the glacier terminus

box [Fig. 5(a)] expressed as the variable X_{diff}

$$X_{\text{diff}} = \frac{\sum_{i=1}^{3} |\vec{X}_{\text{auto}} - \vec{X}_{\text{manual}}|}{3} \tag{6}$$

where $|X_{\text{auto}} - X_{\text{manual}}|$ represents the Euclidean distance between the automatically and manually delineated terminus positions for a given flow line. These flow lines are extrapolated from the quarter points of the left and right sides of the glacier terminus boxes, which are determined from the box vertices using several midpoint calculations [Fig. 5(a)]. The use of three flow lines at varying distances across the glacier's width allows the method to extract terminus positions from delineations that do not span the entire width of the terminus. In addition, patterns in terminus position change are likely to vary closer to the fjord walls versus the middle of the glacier width as the terminus position tends to be more stable along the margins [12]. This strategy could be expanded by calculating the terminus positions along the additional flow lines. Calculating terminus position along three flow lines allows our method to resolve the variability in terminus position change along distinct longitudinal profiles, which is useful for analysis of differences in terminus dynamics due to glacier geometry, velocities, and other factors that vary along the glacier width. In contrast, the box method would evaluate terminus change in terms of a single area-averaged change value [20], [24], [27].

The misfit for each image X_{diff} is averaged for a total of $N = 460$ images in the training data set and divided by F^3, where F is defined as the ratio of the number of intersections with the glacier flow lines (i.e., terminus positions calculated) to the total possible number of intersections ($3N$), in the final cost function

$$\Theta(C_{\text{L}}, C_{\text{m}}, C_{\text{A}}) = \frac{\sum_{i=0}^{N} X_{\text{diff}}}{F^3 N}. \tag{7}$$

The filtering sequence using the thresholds C_{m}, C_{L}, and C_{A} affects the automated delineations of terminus position and thus the misfit. To identify the optimal sequence, we calculated the cost Θ using a range of 0–1 for each of these normalized thresholds, for each combination of filtering order. The sequence that yielded the lowest median cost value was chosen as the optimal order for filtering: average modulus value, length, and then argument. Using this optimal filtering sequence, we computed the costs for combinations of the thresholds C_{m}, C_{L}, and C_{A}. For C_{m}, the cost was minimal at $C_{\text{m}} = 0.7$ for all combinations of C_{L} and C_{A}. Therefore, we set C_{m} to 0.7 and computed costs for a grid of C_{A} and C_{L} values. With C_{m} set to 0.7, cost value was minimal for $C_{\text{A}} = 0.1$ and $C_{\text{L}} = 0.4$ (Fig. 6).

The WTMM chains that do not satisfy the thresholds set above are eliminated. Chains that do not correspond to the glacier terminus (e.g., delineations of long, high-contrast, and vertical features such as shadow boundaries and sea ice margins) may still remain but may be removed when the time series is filtered (see Section II-C). These remaining chains across the 50 scales of analysis are aggregated and the five chains that are most likely to delineate the terminus
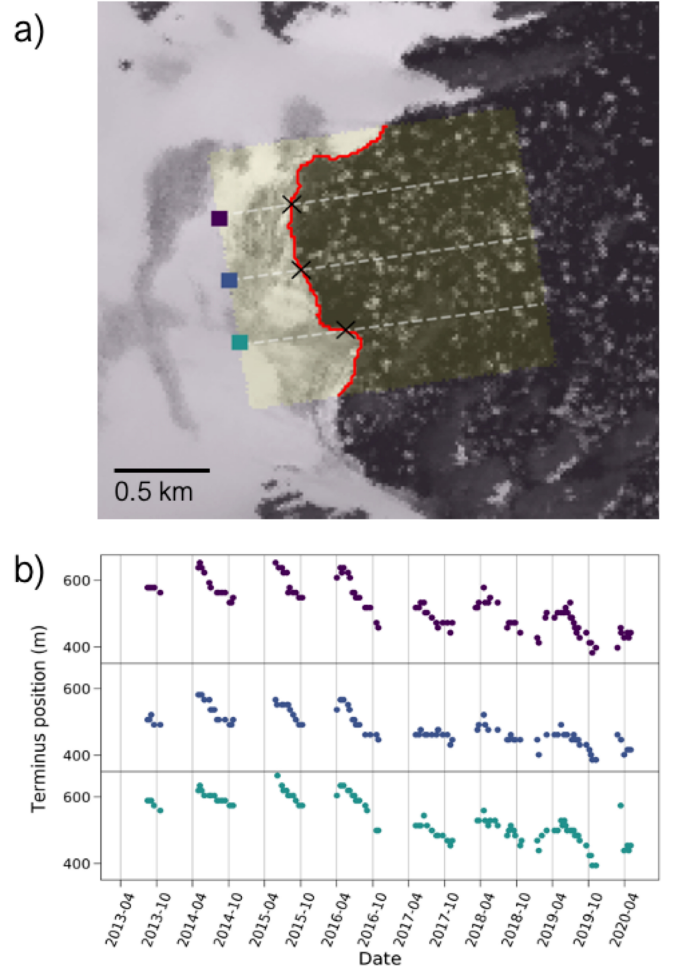

Fig. 5. (a) Three flow lines pulled from points one-quarter, one-half, and three-quarters of the way across the width of the glacier's terminus box (faint yellow). Terminus position is measured along each flow line as the distance between the intersection of the delineation with the flow line (black Xs) and the point on the left side of the box (squares). Landsat 8 image of peripheral glacier RGI50-05.03806 (60.9779° N, 43.3386° W) was acquired on June 16, 2019. (b) Time series of terminus position along the three flow lines over the Landsat 8 record. Slight differences in terminus position change between flow lines are resolved.

are identified based on the metric

$$L \times \frac{m}{2^a} \tag{8}$$

where m is the average modulus value and L is the length, as defined earlier. Average modulus values of the maxima chains increase with scale (2^a) of WTMM analysis [2] so the average modulus value is normalized by the scale. The length of the chain and the scale normalized average modulus value in (8) will both be large for a delineation of the terminus. We choose up to five chains from each image with the highest metric values. If fewer than five chains remain after the thresholding, then all the remaining chains will be identified as the top chains, which will be allowed to pass on to the time series filtering.

C. Constructing Terminus Position Time Series

Using the procedures described above, there are up to five maxima chains that delineate the terminus position in each
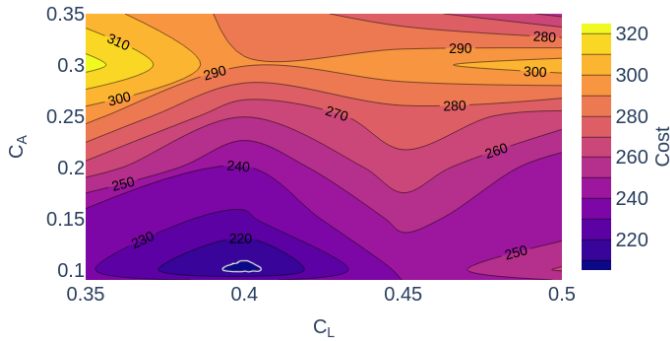
Fig. 6. Contour plot of the cost as a function of length and argument thresholds, C_L and C_A, respectively. C_m is set as 0.7. The white contour is the contour boundary separating the lowest cost interval, located at $C_L = 0.4$ and $C_A = 0.1$.

available satellite image. For each maxima chain, we extract the points of intersection with the three glacier flow lines. These points are then filtered iteratively using terminus change rates calculated as a forward difference using the terminus position of the current time point and the subsequent time point. If the rate of terminus advance calculated from the delineation is three times greater than the maximum glacier speed, this delineation is considered inaccurate and the point is eliminated. Although the glacier terminus cannot advance faster than the rate at which the ice is flowing, we use a conservative threshold of three times the maximum flow speed within the glacier terminus box in order to account for temporal variations in glacier velocities. The same threshold is applied to points that yield a high rate of terminus retreat if followed by the rate of advance that violates the flow speed condition. The filtering is repeated three times; and at each time, the terminus change rates between time points are recalculated. If multiple terminus position points remain for one time point, the point associated with the highest metric value defined in (8) is chosen to represent the terminus position at that time point. Terminus positions along each flow line are filtered separately.

The resulting filtered time series are dense, showing changes in terminus position at subseasonal timescales (Fig. 7). The time series shown in Fig. 7 allow for observation of seasonal glacier retreat from ∼April through ∼October, which is the typical timing of retreat for glaciers in Greenland [11], [26] as well as the overall trend in retreat from 2013 to 2020.

III. EVALUATION OF THE METHOD'S PERFORMANCE

We evaluate our automated method's accuracy in comparison to the data set of manual delineations, with consideration of the various environmental and image conditions shown in Fig. 8 (clear, bright and dim lighting, thin cloud presence, sea ice presence, shadow presence, etc.). We compare the automated–manual differences to manual–manual differences in delineation. The manual–manual differences in terminus positions were determined experimentally from two human analysts delineating the same $n = 50$ images over the five sample glaciers (see Section II-B), including images with each of the conditions listed above. Experiments yielded a standard deviation in the manual delineation of ±31.0 m or ∼2 pixels.
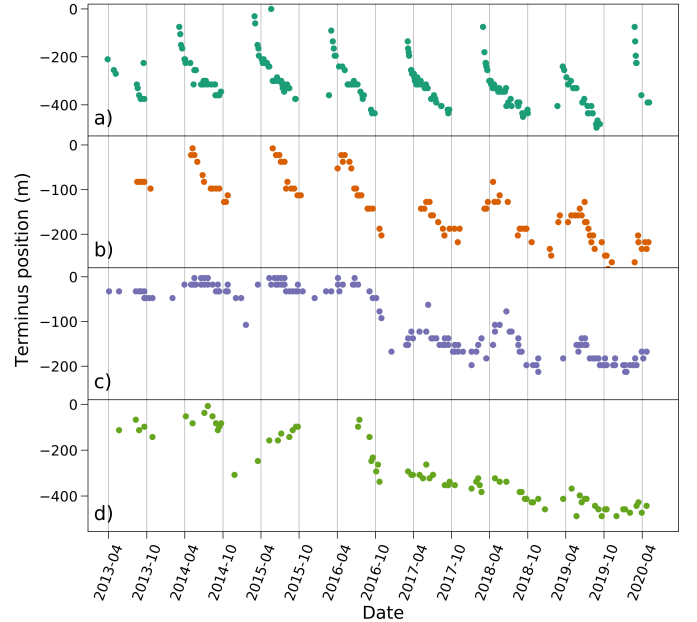

Fig. 7. Time series of terminus position along the center flow line for four of the sample glaciers from automated analysis over the Landsat 8 record (2013–2020). RGI ID and center latitude and longitude for four glaciers shown. (a) RGI50-05.08015 (77.1825° N, 69.9648° W). (b) RGI50-05.08054 (76.8639° N, 67.5921° W). (c) RGI50-05.03806 (60.9779° N, 43.3386° W). (d) RGI50-05.05257 (61.6578° N, 42.7686° W).

TABLE I

MEDIAN MISFIT VALUES (X_{diff}) ± ONE MEDIAN OF ABSOLUTE DIFFERENCE (MAD) BY IMAGE CONDITION FOR THE CROSS-VALIDATION DATA SET ($N = 51$) AND THE FULL DATA SET ($N = 512$). MISFITS ARE AVERAGED FROM FOUR ITERATIONS OF CROSS-VALIDATION

Image condition*	X_{diff} (m)	
	Cross-validation test dataset	Full dataset
CL	14.9 ± 7.8 ($n = 19$)	14.5 ± 10.3 ($n = 217$)
BD	11.3 ± 9.8 ($n = 6$)	10.9 ± 9.8 ($n = 28$)
TC	3.5 ± 1.9 ($n = 4$)	17.2 ± 16.3 ($n = 30$)
SI	72.5 ± 61.2 ($n = 18$)	75.9 ± 34.0 ($n = 206$)
SH	93.9 ± 71.2 ($n = 4$)	25.9 ± 15.2 ($n = 31$)

* Image condition: CL=clear (no cloud cover or sea ice, typical lighting conditions, snow may be present), BD = uniformly bright or dim lighting, TC = thin clouds present, SI = sea ice present, and SH = shadows.

The accuracy of the automated method on an image-by-image basis, referred to from now onward as the point uncertainty, was calculated using the misfit (X_{diff}). Table I shows the median misfits between the automated and manual delineations by image condition for 10% (51 out of the 512—see Section II-B) of manual delineations excluded from the threshold optimization as well as the full manual data set. The cross-validation values in Table I are averaged from four iterations, with different training and testing data sets each time.

Based on these results, the automated method is capable of delineating terminus positions at an accuracy similar to that of manual uncertainties in images that are clear, uniform in brightness (either dim or bright), or contain thin cloud
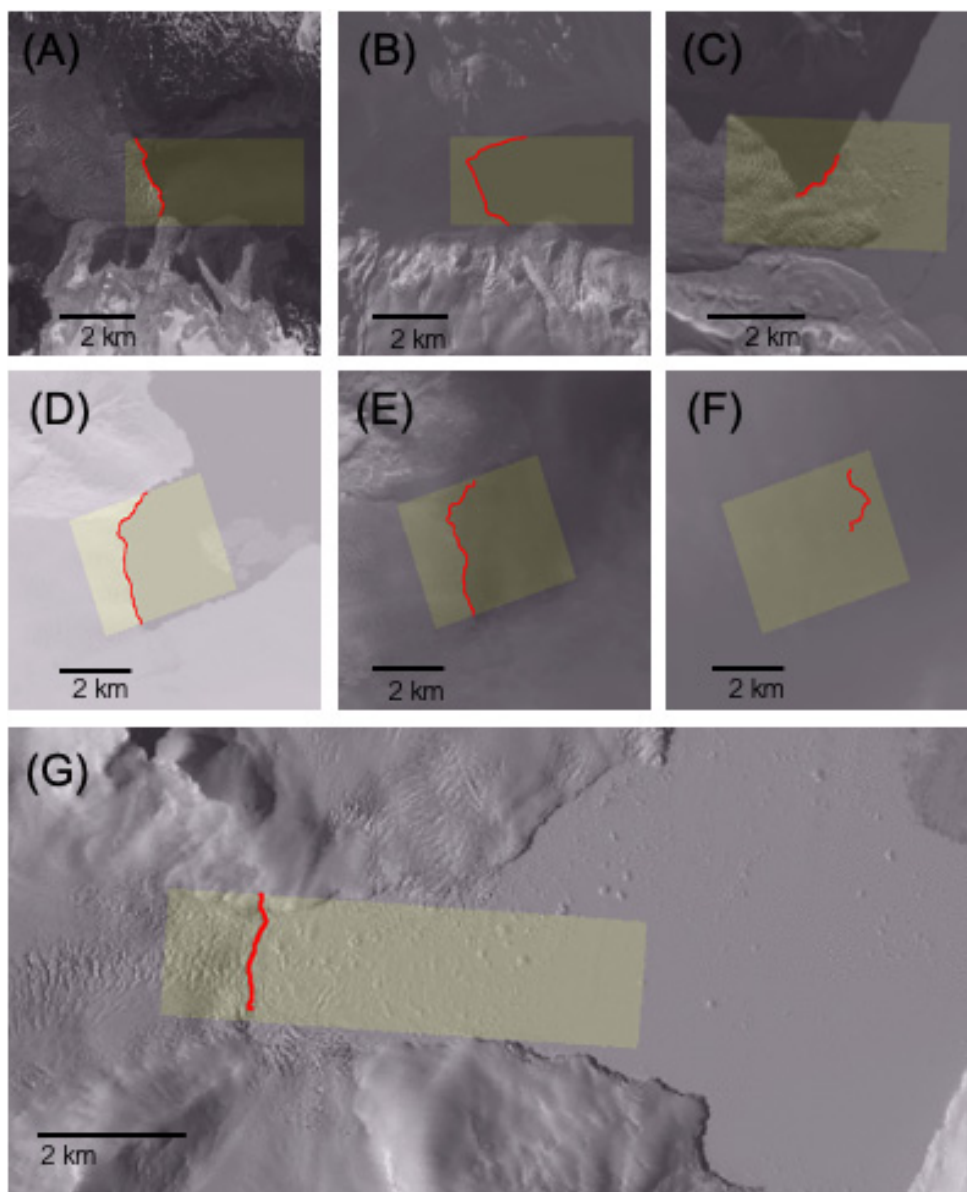
Fig. 8. Examples of automated delineations from a variety of peripheral glaciers and image conditions. Delineations are likely to be accurate for the following image conditions: (a) Clear image with high-intensity contrast between glacier ice and darker ocean water. (b) Dim image. (d) Bright image. (e) Image with thin cloud cover present. The following conditions present challenges to delineation: (c) partial shadow near calving front and (f) thick cloud cover present. Automated delineation yields mixed results for (g) images with sea ice in front of the terminus. (a) and (b) are Landsat 8 images over peripheral glacier RGI50-05.00460 (65.9493° N, 51.3711° W), (c) is of glacier RGI50-05.08041 (76.9672° N, 68.7804° W), (d)–(f) are of RGI50-05.05257 (61.6578° N, 42.7686° W), and (g) is of glacier RGI50-05.07192 (64.0291° N, 41.0122° W).

cover (Table I). For clear images, where there is high contrast between the glacier ice and open water [e.g., Fig. 8(a)], the automated method effectively delineates terminus positions within 1-pixel uncertainty from the manual delineations. Due to the method's gradient-based algorithm, it also effectively delineates glacier terminus positions in images that are uniformly bright or dim [Fig. 8(b) and (d)] and where thin clouds are present [Fig. 8(e)], with better than 1-pixel uncertainty. The median misfit for these three image conditions was 12.5 ± 7.5 m or <1 pixel. The automated method's point uncertainty for these image conditions is within the interanalyst uncertainty in delineation of ∼2 pixels.

Images where the fjord walls cast shadows across the glacier terminus, producing a higher intensity gradient than

the gradient along the terminus, delineations are often along the shadow boundary [Fig. 8(c)]. In addition, the method may delineate the shadow cast from the ice cliff at the calving front onto the sea ice. For the latter condition, the distance between the glacier terminus and the delineated shadow from the ice cliff will be greater when the incident angle of the sunlight is greater and will depend on the glacier's aspect. North-facing glaciers are particularly susceptible to these inaccuracies. If the ice cliff shadow is delineated using the automated method, then the movement of the shadow with the gradual change in sun angle over time may result in a false decrease in terminus position prior to the start of the actual glacier retreat in April, as seen in the time series shown in Fig. 7(a). It may be possible to correct for the shadow offset using the time of

acquisition of the image, the viewing angle of the satellite, and precise knowledge of the surrounding terrain; but we do not explore these more complex methods here. Terminus positions delineated during low sun angle months at high latitudes should be interpreted with caution, but the automated delineations are robust for delineations in less challenging lighting conditions.

Sea ice breakup can complicate the delineation of the terminus boundary. The automated method can delineate the terminus boundary when there is sea ice that is cohesive and extends out of the terminus box [Fig. 8(g)]. However, sea ice breakup within the terminus box can present a challenge to delineation, since the high contrast between the bright sea ice and open water is often higher than the contrast between glacier ice and sea ice. For glaciers where gradual seasonal sea ice or mélange breakup is prominent, the automated method may delineate boundaries that are further out than the glacier terminus. Due to our selection of top five maxima chains and our time series filtering using glacier velocities, these false advances are often filtered out. The standard glacier velocity threshold of three times the maximum flow speed could be made stricter (e.g., 1 or 2 times the maximum flow speed) for more stringent time series filtering. However, lowering the glacier velocity threshold results in a tradeoff between the improvement in time series for these glaciers and a loss of temporal resolution for glaciers with large uncertainties in velocity, which are overfiltered as a result. In the absence of accurate, high spatial resolution time series of ice velocity, we recommend using the large standard threshold of three times the maximum flow speed and performing additional time series filtering outside the algorithm.

Snow cover is another seasonal condition that may influence the method performance. Snow covering the boundary between glacier ice and sea ice may greatly reduce the intensity contrast across the terminus boundary. In addition, spatial variability in snow covering the glacier ice Fig. 5(a) may create intensity gradients within the glacier margins that are greater than the gradients across the terminus boundary. Delineation of nonglacial snow margins will likely be similar to those corresponding to noisy features (shorter in length and variable in orientation) which would be filtered out during the thresholding process. In cases where the method does not accurately resolve the terminus boundary, the calculated terminus positions may also be filtered out through the time series filtering steps discussed in Section II-C.

As the glaciers retreat and advance, the movement of the glacier terminus outside the terminus box and to new positions along the fjords with variable orientations is possible. The glacier terminus boxes were drawn to encompass the glaciers' terminus positions in 2000 and 2015, accounting for the retreat along the fjords. Therefore, few adjustments to the box length or orientation were necessary for our analysis over the Landsat 8 record from 2013 to 2020. However, outside the 2000–2015 time period, the terminus may retreat or advance to a position in the fjord outside of the box and potentially exhibit a different orientation. In these cases, the terminus boxes will require adjustment, which can be implemented automatically using ice velocity vectors to determine glacier orientations along the fjord as well as a window in which the terminus position movement is possible.

Despite the number of temporal variations and environmental conditions that may challenge the method's ability to delineate glacier front positions, our method is able to produce dense time series of frontal positions. These time series resolve glacier length changes at subseasonal timescales and at numerous locations across the glacier width, which will allow for the detailed analysis of the length and the terminus geometry change in conjunction with the time series of glacier dynamics

IV. CONCLUSION

The use of the adapted 2-D WTMM segmentation method for delineation of glacier calving fronts is promising. This automated method is capable of delineating marine glacier calving fronts within 1-pixel uncertainty in images with clear conditions, dim or bright lighting conditions, and thin cloud presence. Images where there are shadows cast by the fjord walls across the glacier terminus and where there are shadows from the ice cliff at the calving front remain challenging to delineate using this method. However, knowing that two humans do not produce identical delineation lines, our experiments show that the automated method has an uncertainty that is within the interhuman variability. This automated method can be applied to accurately and efficiently resolve subseasonal to multiyear patterns in the glacier terminus position change in a variety of image conditions.

The resulting time series of glacier terminus position generated from this method can be used to assess glacier calving front shape changes as well as spatiotemporal patterns in glacier length change. We have shown that the time series are able to capture a range of glacier behavior including gradual advances and retreats, calving, and changes in terminus shape. Immediate future work will focus on extending the workflow to include images from earlier Landsat missions such as Landsat 7 and Landsat 5. Future work should explore its application to other image types (satellite radar images and other optical images such as Sentinel-2, etc.), in other regions, and for delineations of other features such as coastlines or closed features such as icebergs and lakes. Adaptation of the method to analyze satellite radar images could be particularly useful for increasing the temporal resolution of these terminus position time series, as radar images are not hindered by cloud presence or darkness in polar night. The code used for all image analyses discussed is available in a GitHub repository (https://github.com/julialiu18/automated-glacier-terminus).

REFERENCES

[1] T. C. Bartholomaus *et al.*, "Contrasts in the response of adjacent fjords and glaciers to ice-sheet surface melt in West Greenland," *Ann. Glaciol.*, vol. 57, no. 73, pp. 25–38, May 2016, doi: 10.1017/aog.2016.19.

[2] K. A. Batchelder *et al.*, "Wavelet-based 3D reconstruction of microcalcification clusters from two mammographic views: New evidence that fractal tumors are malignant and Euclidean tumors are benign," *PLoS ONE*, vol. 9, no. 9, Sep. 2014, Art. no. e107580.

[3] J. R. Carr, C. R. Stokes, and A. Vieli, "Recent progress in understanding marine-terminating Arctic outlet Glacier response to climatic and oceanic forcing: Twenty years of rapid change," *Prog. Phys. Geography*, vol. 37, no. 4, pp. 436–467, 2013, doi: 10.1177/0309133313483163.

[4] G. A. Catania, L. A. Stearns, T. Moon, E. Enderlin, and R. H. Jackson, "Future evolution of Greenland's marine-terminating outlet Glaciers," *J. Geophys. Res.: Earth Surf.*, vol. 125, no. 2, 2020, Art. no. e2018JF004873, doi: 10.1029/2018JF004873.

[5] A. J. Cook, P. R. Holland, M. P. Meredith, T. Murray, A. Luckman, and D. G. Vaughan, "Ocean forcing of Glacier retreat in the Western Antarctic Peninsula," *Science*, vol. 353, no. 6296, pp. 283–286, 2016, doi: 10.1126/science.aae0017.

[6] A. J. Cook *et al.*, "Atmospheric forcing of rapid marine-terminating Glacier retreat in the Canadian Arctic Archipelago," *Sci. Adv.*, vol. 5, no. 3, Mar. 2019, Art. no. eaau8507, doi: 10.1126/sciadv.aau8507.

[7] E. M. Enderlin *et al.*, "An improved mass budget for the Greenland ice sheet," *Geophys. Res. Lett.*, vol. 41, no. 3, pp. 866–872, 2014, doi: 10.1002/(ISSN)1944-8007.

[8] A. S. Gardner *et al.*, "A reconciled estimate of Glacier contributions to sea level rise: 2003 to 2009," *Science*, vol. 340, no. 6134, pp. 852–857, May 2013, doi: 10.1126/science.1234532.

[9] J. Grant *et al.*, "Perinuclear distribution of heterochromatin in developing C. Elegans embryos," *Chromosome Res.*, vol. 18, no. 8, pp. 873–885, Dec. 2010.

[10] I. M. Howat, I. Joughin, S. Tulaczyk, and S. Gogineni, "Rapid retreat and acceleration of Helheim glacier, East Greenland," *Geophys. Res. Lett.*, vol. 32, no. 22, 2005, Art. no. L22502, doi: 10.1029/2005GL024737.

[11] I. M. Howat, J. E. Box, Y. Ahn, A. Herrington, and E. M. McFadden, "Seasonal variability in the dynamics of marine-terminating outlet glaciers in Greenland," *J. Glaciol.*, vol. 56, no. 198, pp. 601–612, 2010.

[12] I. M. Howat, I. Joughin, M. Fahnestock, B. E. Smith, and T. Scambos, "Synchronous retreat and acceleration of southeast Greenland outlet glaciers 2000–06: Ice dynamics and coupling to climate," *J. Glaciol.*, vol. 54, no. 187, pp. 646–660, 2008, doi: 10.3189/002214308786570908.

[13] *Climate Change 2014: Synthesis Report. Contribution of Working Groups I, II and III to the Fifth Assessment Report of the Intergovernmental Panel on Climate Change*, R. K. Pachauri and L.A. Meyer, Eds. IPCC, Geneva, Switzerland, 2014, p. 151.

[14] I. Joughin, B. E. Smith, and I. M. Howat, "A complete map of Greenland ice velocity derived from satellite data collected over 20 years," *J. Glaciol.*, vol. 64, no. 243, pp. 1–11, Feb. 2018, doi: 10.1017/jog.2017.73.

[15] I. Joughin, B. Smith, I. Howat, and T. Scambos, "MEaSUREs multi-year Greenland ice sheet velocity mosaic, version 1," NASA Nat. Snow Ice Data Center Distrib. Act. Arch. Center, Boulder, CO, USA, Tech. Rep., 2016, doi: 10.5067/QUA5Q9SVMSJG.

[16] P. Kestener *et al.*, "Characterising complexity in compound systems: Segmentation in wavelet-space," *Astrophys. J.*, vol. 717, pp. 995–1005, Feb. 2010.

[17] A. Khalil, J. L. Grant, L. B. Caddle, E. Atzema, K. D. Mills, and A. Arneodo, "Chromosome territories have a highly nonspherical morphology and nonrandom positioning," *Chromosome Res.*, vol. 15, no. 7, pp. 899–916, Nov. 2007.

[18] M. D. King *et al.*, "Dynamic ice loss from the Greenland ice sheet driven by sustained glacier retreat," *Commun. Earth Environ.*, vol. 1, no. 1, Dec. 2020, doi: 10.1038/s43247-020-0001-2.

[19] M. D. King *et al.*, "Seasonal to decadal variability in ice discharge from the Greenland ice sheet," *Cryosphere*, vol. 12, no. 12, pp. 3813–3825, Dec. 2018, doi: 10.5194/tc-12-3813-2018.

[20] J. M. Lea, D. W. F. Mair, and B. R. Rea, "Evaluation of existing and new methods of tracking glacier terminus change," *J. Glaciol.*, vol. 60, no. 220, pp. 323–332, 2014.

[21] B. Li, A.-X. Zhu, Y. Zhang, T. Pei, C. Qin, and C. Zhou, "Glacier change over the past four decades in the middle Chinese Tien Shan," *J. Glaciol.*, vol. 52, no. 178, pp. 425–432, 2006.

[22] Z. Marin, J. K. Wallace, J. L. Nadeau, and A. Khalil, "Wavelet-based tracking of bacteria in unreconstructed off-axis holograms," *Methods*, vol. 136, pp. 60–65, Mar. 2017, doi: 10.1016/j.ymeth.2017.09.003.

[23] R. T. J. McAteer, P. Kestener, A. Arneodo, and A. Khalil, "Automated detection of coronal loops using a wavelet transform modulus maxima method," *Sol. Phys.*, vol. 262, no. 2, pp. 387–397, Apr. 2010.

[24] R. W. McNabb and R. Hock, "Alaska tidewater Glacier terminus positions, 1948–2012," *J. Geophys. Res.: Earth Surf.*, vol. 119, no. 2, pp. 153–167, 2014, doi: 10.1002/2013JF002915.

[25] E. M. McFadden, I. M. Howat, I. Joughin, B. E. Smith, and Y. Ahn, "Changes in the dynamics of marine terminating outlet glaciers in West Greenland (2000–2009)," *J. Geophys. Res.: Earth Surf.*, vol. 116, no. F2, 2011, Art. no. F02022, doi: 10.1029/2010JF001757.

[26] T. Moon, I. Joughin, and B. Smith, "Seasonal to multiyear variability of glacier surface velocity, terminus position, and sea ice/ice Mélange in northwest Greenland," *J. Geophys. Res.: Earth Surf.*, vol. 120, no. 5, pp. 818–833, 2015, doi: 10.1002/2015JF003494.

[27] T. Moon and I. Joughin, "Changes in ice front position on Greenland's outlet glaciers from 1992 to 2007," *J. Geophys. Res.*, vol. 113, no. F2, 2008, Art. no. F02022, doi: 10.1029/2007JF000927.

[28] B. Nishizawa *et al.*, "Contrasting assemblages of seabirds in the subglacial meltwater plume and oceanic water of Bowdoin fjord, northwestern Greenland," *ICES J. Mar. Sci.*, vol. 77, no. 2, pp. 711–720, 2020, doi: 10.1093/icesjms/fsz213.

[29] R. Nijhawan and K. Jain, "Glacier terminus position monitoring and modelling using remote sensing data," in *Advances in Computing and Data Sciences*, vol. 906. Singapore: Springer, 2018, doi: 10.1007/978-981-13-1813-9_2.

[30] B. Noël *et al.*, "A tipping point in refreezing accelerates mass loss of Greenland's glaciers and ice caps," *Nature Commun.*, vol. 8, p. 14730, Mar. 2017, doi: 10.1038/ncomms14730.

[31] A. E. Racoviteanu, M. W. Williams, and R. G. Barry, "Optical remote sensing of glacier characteristics: A review with focus on the Himalaya," *Sensors*, vol. 8, no. 5, pp. 3355–3383, 2008, doi: 10.3390/s8053355.

[32] B. Raup *et al.*, "Remote sensing and GIS technology in the global land ice measurements from space (GLIMS) project," *Comput. Geosci.*, vol. 33, no. 1, pp. 104–125, Jan. 2007, doi: 10.1016/j.cageo.2006.05.015.

[33] T. Roland *et al.*, "Revisiting the physical processes of vapodeposited thin gold films on chemically modified glass by atomic force and surface plasmon microscopies," *Surf. Sci.*, vol. 603, no. 22, pp. 3307–3320, Nov. 2009.

[34] A. Seale, P. Christoffersen, R. I. Mugford, and M. O'Leary, "Ocean forcing of the greenland ice sheet: Calving fronts and patterns of retreat identified by automatic satellite monitoring of eastern outlet glaciers," *J. Geophys. Res.*, vol. 116, no. F3, 2011, Art. no. F03013, doi: 10.1029/2010JF001847.

[35] D. Selkowitz and R. Forster, "Automated mapping of persistent ice and snow cover across the Western U.S. with Landsat," *ISPRS J. Photogramm. Remote Sens.*, vol. 117, pp. 126–140, Jul. 2016, doi: 10.1016/j.isprsjprs.2016.04.001.

[36] T. F. Stocker *et al.*, *Technical Summary, Climate Change 2013: The Physical Science Basis. Contribution of Working Group I to the Fifth Assessment Report of the Intergovernmental Panel on Climate Change*, T. F. Stocker, D. Qin, G.-K. Plattner, M. Tignor, S. K. Allen, J. Boschung, A. Nauels, Y. Xia, V. Bex and P. M. Midgley, Eds. Cambridge, U.K.: Cambridge Univ. Press, 2013.

[37] F. Straneo *et al.*, "Impact of fjord dynamics and glacial runoff on the circulation near Helheim glacier," *Nature Geosci.*, vol. 4, pp. 322–327, Mar. 2011, doi: 10.1038/ngeo1109.

[38] M. R. van den Broeke *et al.*, "On the recent contribution of the greenland ice sheet to sea level change," *Cryosphere*, vol. 10, no. 5, pp. 1933–1946, Sep. 2016, doi: 10.5194/tc-10-1933-2016.

Julia Liu received the B.A. degree in environmental Earth science from Dartmouth College, Hanover, NH, USA, in 2018, and the M.S. degree in geophysics from Boise State University, Boise, ID, USA, in 2020, where she is pursuing the Ph.D. degree in geophysics.

From 2017 to 2018, she worked as an Intern with the U.S. Army Corps of Engineers Cold Regions Research and Engineering Laboratory (CRREL), Hanover, performing geographic information systems (GIS) analysis in support of the Greenland inland traverse operations. She worked with the Dartmouth Ice Core Laboratory, Hanover, NH, USA, processing ice cores collected from Greenland and the South Pole. From 2018 to 2019, she was a Research Assistant with the Physical Glaciology and Remote Sensing Group and the Computational Modeling, Analysis of Images, and Numerical Experiments (CompuMAINE) Laboratory, University of Maine, Orono, ME, USA. She works as a Research Assistant with the Department of Geosciences, Boise State University.

Ms. Liu is a member of the American Geophysical Union and the International Glaciological Society.

Ellyn M. Enderlin received the B.S. degree in environmental science from Lehigh University, Bethlehem, PA, USA, in 2008, and the M.S. degree in geological sciences and the Ph.D. degree in Earth sciences from The Ohio State University, Columbus, OH, USA, in 2010 and 2013, respectively.

From 2013 to 2014, she was a Post-Doctoral Researcher with the University of Maine, Orono, ME, USA, where she was a Research Assistant Professor from 2014 to 2019. She is an Assistant Professor with Boise State University, Boise, ID, USA. She has authored a number of articles on glaciers and remote sensing, including *Evolving Environmental and Geometric Controls on Columbia Glacier's Continued Retreat* (*Journal of Geophysical Research: Earth Surface*, 2018), *Iceberg Meltwater Fluxes Dominate the Freshwater Budget in Greenland's Glacial Fjords* (*Geophysical Research Letters*, 2016), and *An Improved Mass Budget for the Greenland Ice Sheet* (*Geophysical Research Letters*, 2014). She is interested in developing novel methods for investigating the response of glaciers to climate change, with an emphasis on the use of remote sensing data to study the changing ice–ocean interactions and glacier dynamics.

Dr. Enderlin is a member of the American Geophysical Union and the International Glaciological Society.

Hans-Peter Marshall received the B.S. degree in physics (with a minor in geophysics) from the University of Washington, Seattle, WA, USA, in 1999, and the Ph.D. degree in civil engineering (with an emphasis in geotechnical engineering) from the University of Colorado at Boulder, Boulder, CO, USA, in 2005.

He was with the Swiss Federal Institute for Snow and Avalanche Research, Davos, Switzerland, as a Visiting Ph.D. Student, in 2004. He is an Associate Professor with the Department of Geosciences and the Director of the Cryosphere Geophysics and Remote Sensing Group, Boise State University, Boise, ID, USA, and also a Consultant for the U.S. Army Cold Regions Research and Engineering Laboratory, Hanover, NH, USA. He is a Snow Scientist and a Glaciologist who uses geophysics and engineering tools to study the Cryosphere, and is the Project Scientist of the NASA SnowEx Mission (2019–2021). His research interests include spatial variability in snow and its effect on remote sensing, snow hydrology, and snow avalanches.

Dr. Marshall was a recipient of the 2010 AGU Cryosphere Focus Group's Young Investigator Award, the U.S. Young Scientist Award from the International Union of Radio Science (URSI) in 2008, and the University of Washington's Timeless Award in 2012. He has performed snow research in Antarctica, Greenland, Arctic Canada, and throughout the mountains of the Western U.S.

Andre Khalil received the B.S. and M.S. degrees in mathematics from Concordia University, Montreal, QC, Canada, in 1996 and 1999, respectively, and the Ph.D. degree in mathematics and astrophysics from Universite Laval, Quebec, QC, Canada, in 2004.

From 2004 to 2005, he was a Post-Doctoral Fellow with Jackson Laboratory, Bar Harbor, ME, USA. From 2005 to 2017, he was an Assistant Professor and then an Associate Professor of Mathematics with the University of Maine, Orono, ME. In 2018, he switched from the Department of Mathematics and Statistics to the Department of Chemical and Biomedical Engineering with the University of Maine, where he is a Professor of Biomedical Engineering. He has coauthored over 60 publications in astrophysics, surface science, mathematics, cellular and molecular biology, astrobiology, neuroscience, physiology, and cancer research. He holds a patent on *Improved Methods of Cancer Detection*.